

Spatial polarization gating of high-harmonic generation in solids

Pieter J. van Essen ^{1,*} Brian de Keijzer ¹ Tanya van Horen ¹ Eduardo B. Molinero ²
 Álvaro Jiménez Galán ^{2,3} Rui. E. F. Silva ^{2,3} and Peter M. Kraus ^{1,4,†}

¹*Advanced Research Center for Nanolithography, Science Park 106, NL-1098 XG Amsterdam, The Netherlands*

²*Instituto de Ciencia de Materiales de Madrid, Consejo Superior de Investigaciones Científicas (ICMM-CSIC), E-28049 Madrid, Spain*

³*Max-Born-Institute for Nonlinear Optics and Short Pulse Spectroscopy, Max-Born-Strasse 2A, D-12489 Berlin, Germany*

⁴*Department of Physics and Astronomy, and LaserLaB, Vrije Universiteit, De Boelelaan 1105, NL-1081 HV Amsterdam, The Netherlands*



(Received 8 August 2024; accepted 5 February 2025; published 11 March 2025)

High-harmonic generation from solids can be utilized as a probe of ultrafast dynamics, but thus far only over extended sample areas, since its spatial resolution is diffraction limited. Here, we propose spatial polarization gating, that is, using a spatially varying ellipticity of a driving laser pulse to reduce the spatial profile of high-harmonic emission below the diffraction limit and hence increase spatial resolution. We show experimentally and by numerical simulations that our method is generally applicable as suppressing high harmonics in elliptical fields is a common response in all solids. We also briefly explore the possibility of applying this technique to wide-field imaging, specifically to nonlinear structured illumination microscopy. Our findings indicate that spatial polarization gating can enable all-optical femto-to-attosecond label-free imaging beyond the Abbe limit.

DOI: [10.1103/PhysRevResearch.7.L012063](https://doi.org/10.1103/PhysRevResearch.7.L012063)

A plethora of recent works have demonstrated high-harmonic generation (HHG) as a highly sensitive probe for ultrafast phenomena in solids [1–8], such as the detection of electron dynamics [1,2], coherent phonons [3], and material phase transitions [4,5] with in principle subcycle (i.e., few to sub-fs) temporal resolution [2,9]. Although recent studies have mostly focused on homogeneous samples there is an exciting prospect in spatially resolving these dynamics in systems such as semiconductor devices, nanophotonic metasurfaces, and microscopic flakes. Complicating the imaging of these devices is the fact that their feature size can be well below the wavelength of visible light. HHG is inherently sensitive to nanostructures [10] and structural details below the driving wavelength [11] can modulate the conversion efficiency. The diffraction-limited nature of light in combination with the relatively long wavelengths required for HHG in solids means that simply combining HHG with conventional microscopy will not yield the required resolution for imaging these microscopic systems.

To overcome the diffraction limit, superresolution imaging techniques have been developed, which are widely used in bio(medical) imaging [12]. Examples of superresolution techniques include stimulated depletion microscopy (STED) [13,14], photoactivated localization microscopy (PALM) [15], and stochastic optical reconstruction microscopy (STORM)

[16]. These techniques rely on specific properties of fluorescence, as such they cannot simply be applied to HHG imaging.

Recently, the first superresolution imaging technique based on the properties of HHG from solids was demonstrated [17]. This harmonic depletion microscopy (HADES) shares similarities with STED as HHG emission is inhibited by an orbital-angular-momentum carrying preexcitation pulse. Here, we will exploit the strong dependence of the HHG process on the specific properties of the driving field to spatially confine HHG below the diffraction limit in a material-independent and thus generally applicable way.

We propose to obtain a high spatial resolution for HHG imaging using ellipticity to control emission via spatial polarization gating (SPG). SPG is inspired by attosecond (temporal) polarization gating [18], the first technique that was proposed to generate isolated attosecond pulses in the extreme-ultraviolet spectral range via HHG from gases. In polarization gating, a half-cycle overlap of two counterrotating circularly polarized femtosecond pulses facilitates temporally confining HHG and thus enables the generation of isolated attosecond pulses [19]. Spatial confinement of third-harmonic generation using a driver with spatially varying ellipticity has been demonstrated [20]. Here, we show the general applicability of SPG to HHG in solids, provide a simple framework that allows us to predict the spatial emission profile, and propose an extension of SPG to wide-field imaging.

We measured the ellipticity response of HHG from ZnO, silicon, and sapphire (for details, see Supplemental Material [21]). In all cases, HHG suppression can be described by a Gaussian, matching with the theoretical results of Ref. [32] and qualitatively consistent with HHG in gases [33],

$$\frac{I(\epsilon)}{I(0)} = S(\epsilon) = e^{-\frac{1}{2}(\frac{\epsilon}{\epsilon_0})^2}. \quad (1)$$

*Contact author: p.vessen@arcnl.nl

†Contact author: p.kraus@arcnl.nl

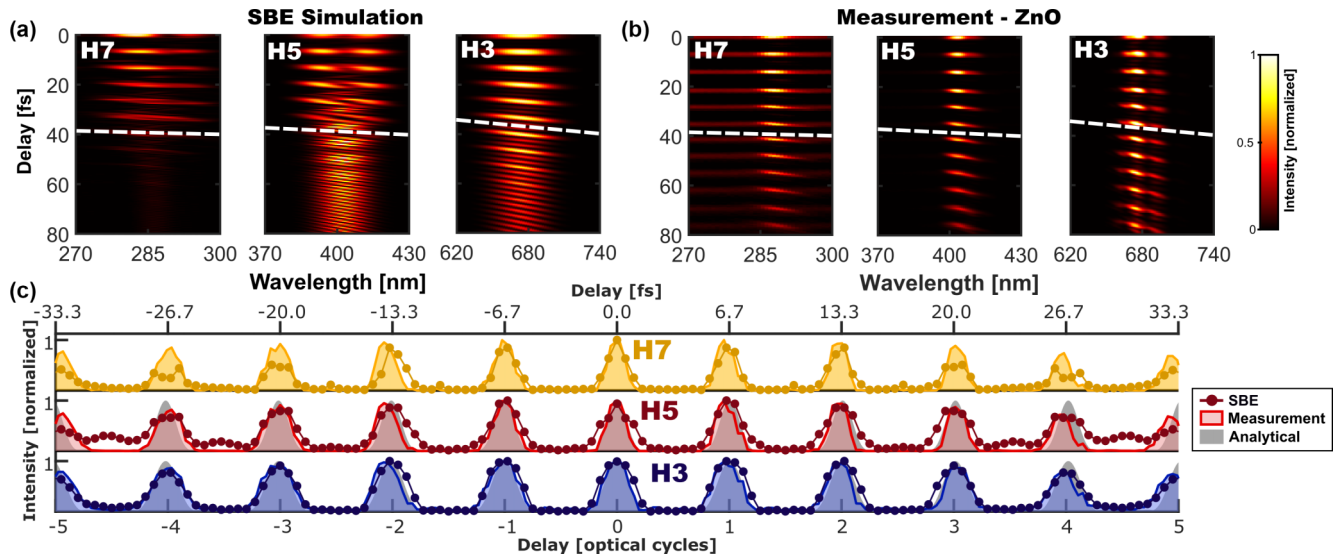


FIG. 1. (a) SBE simulations and (b) experiments in ZnO for harmonics H3–H7 show an intensity modulation as a function of changing delay (phase) between two 2000-nm orthogonally polarized (*s*- and *p*-polarized) pulses. This scan maps delay to ellipticity. HHG emission in the diagonal polarization direction is selected and shown here. The white dashed lines all have the same slope and indicate the spectral tilt. (c) Integrated harmonic intensity for both the SBE simulation and measurement. For H3 and H5 also the analytical results using Eq. (2) with the measured suppression parameters are shown. The top axis corresponds to the simulated delay times.

Here, ϵ is the ellipticity (for a detailed definition, see Supplemental Material [21]), and ϵ_0 specifies the efficiency of suppression. ϵ_0 is larger for higher orders [$\epsilon_0(\text{H3}) = 0.32 \pm 0.02$, $\epsilon_0(\text{H5}) = 0.23 \pm 0.02$] but shows little to no intensity and material dependence. A simple analytical model to predict the harmonic emission considers the harmonic intensity projected along the polarization direction $\hat{\mathbf{r}}$,

$$I_{n,\hat{\mathbf{r}}}(\epsilon) = |\mathbf{E}_n \cdot \hat{\mathbf{r}}|^2 \propto S(\epsilon) \frac{|\mathbf{E}_0 \cdot \hat{\mathbf{r}}|^2}{|\mathbf{E}_0|^2} |\mathbf{E}_0|^{2n}. \quad (2)$$

Here, n denotes the harmonic order, and \mathbf{E}_0 is the incoming electric field. First is the suppression factor $S(\epsilon)$. The second term results from the assumption that the polarization of the HHG emission is the same as that of the incoming light, this assumes perfect momentum conservation between the incoming and emitted light and is typically realized for amorphous and polycrystalline samples. The third term describes the intensity scaling of the harmonic with the incoming intensity, which we treat by perturbation theory. This assumption will fail for higher intensities and orders where nonperturbative (and typically lower) intensity scalings are observed [34]. For the experiments in this Letter, these assumptions were found to hold up.

To support the generality of these observations, we performed simulations of the ZnO ellipticity response by solving the semiconductor Bloch equations (SBEs) [35,36]. We have used a simple tight-binding model to describe the ZnO (for details, see Supplemental Material [21]). Here, the ellipticity is varied by delaying two equally intense 2000-nm pulses with linear and orthogonal polarizations. For these scans, we isolate emission with a polarizer that is aligned diagonally to the *s* and *p* directions.

The simulation results are shown in Fig. 1(a) where we observe periodic suppression of all the harmonics orders. As the delay is scanned over the length of one

fundamental wavelength, the driver ellipticity switches from diagonal linear (maximum HHG) to right-handed circular (full HHG suppression) to antidiagonal linear (maximum HHG), linear polarization of driver rotated by 90° with respect to diagonal) to left-handed circular (full HHG suppression) and back to diagonal linear. As we filter out the antidiagonal emission this leaves us with emission maxima when the delay is a multiple of the wavelength. For longer delays partial pulse overlap results in both reduced HHG emission for linear and reduced suppression for circular polarization. Comparing our SBE simulations with the measurements of ZnO shown in Fig. 1(b), where the ellipticity has similarly been varied by delaying two orthogonally polarized pulses, we observe the same behavior: strong enhancement and suppression with a periodicity matching that of the driving wavelength. The pulse duration in the experiments is longer than in the SBE simulation, resulting in slower intensity changes over the delay scan and spectrally narrower HHG emission. The weak spectrally broad lines observed in addition to the experimental H7 emission can be attributed to the broadband band-gap fluorescence found in ZnO [37], the underlying multiphoton excitation of which also exhibits a strong ellipticity dependence. We also note a spectral tilt in all the harmonic emission maxima, which is due to the difference in phase between the different spectral components in the driving pulse for a given delay. Since this depends on the phases of the driver, the same spectral tilt is found between all the harmonics at a given delay, as illustrated via the dashed white lines which all have the same slope.

The integrated harmonic intensities are shown in Fig. 1(c), together with the analytical model (for H3–H5) using Eq. (2). We observe good agreement between SBE simulation, measurement, and analytical model. The fact that our simulations can reproduce our experimental results while using a tight-binding model instead of specific material properties indicates that even in solids the decreased HHG efficiency for increased

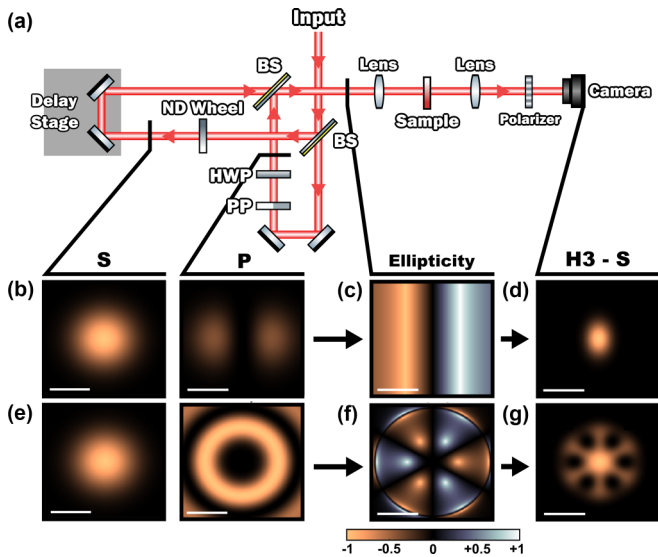


FIG. 2. (a) Setup for SPG. The input beam is separated by a beam splitter (BS). In one of the arms, the spatial profile of the beam is changed via a phase plate (PP) and its polarization is changed with a half-wave plate (HWP). Subsequently, the beams are recombined and focused onto the sample. A delay stage and attenuation wheel are used to tune the relative phase and intensity between the two arms. The harmonic emission is imaged with a camera. The polarization of the detected emission is filtered by a polarizer. (b)–(g) Calculated examples of SPG. (b) and (e) show profiles of the beams in the two arms. The spatial profiles of the p -polarized fields are (b) HG_{10} and (e) LG_{31} . (c) and (f) show the ellipticity after the recombination of the two beams. (d) and (g) show the H3 emission projected onto the s -polarization direction. White scale bars indicate the waist radius of the Gaussian driving field.

ellipticity is a general effect that is strongly governed by the properties of the driving field.

So far we have considered HHG by drivers with uniform ellipticity, and now we will move to SPG, where we consider beams with spatially varying ellipticity. We make use of the setup as shown in Fig. 2(a). An incoming beam is separated into two arms in one of which the polarization is rotated using a half-wave plate (HWP). The relative spatial profile of the beams in the two arms can now be altered with the use of phase plates, which, when recombining the beams, enables the creation of beams with spatially varying ellipticity. In our calculations and experiments, we have focused on propagation stable excitation profiles, in particular, Hermite-Gaussian [HG_{mn} , Figs. 2(b)–2(d)] and Laguerre-Gaussian [LG_{lp} , Figs. 2(e)–2(g)] modes [38]. HG profiles have rectangular symmetry and a phase profile consisting of discrete steps, while the LG profiles have radial symmetry with a phase profile that continuously varies in the azimuthal direction.

To evaluate the spatial HHG emission profiles, we use the analytical model described by Eq. (2) and use the Gaussian suppression with the experimentally found parameters for H3 and H5. Examples of calculated SPG emission profiles are shown in Figs. 2(d) and 2(g). While Fig. 2(d) shows a narrow HHG emission spot, Fig. 2(g) illustrates the possibility of creating more complex emission patterns. These calculations

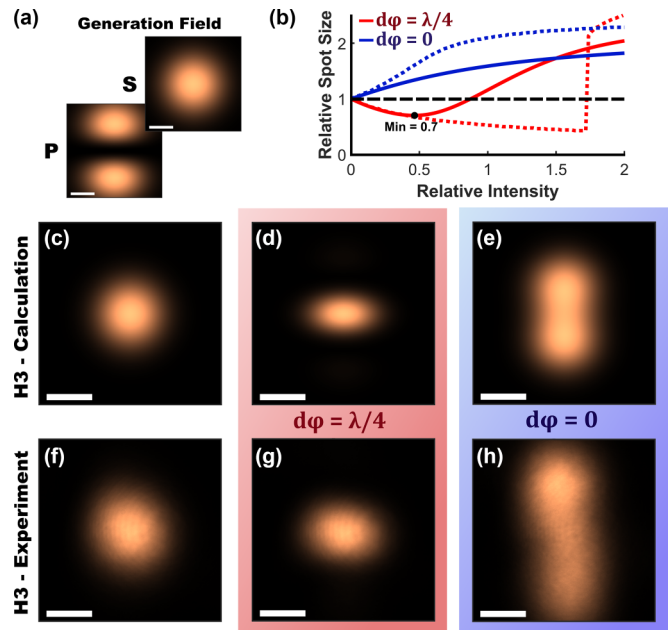


FIG. 3. (a)–(e) Calculations and (f)–(h) measurements of SPG using an 1800-nm driver where the s -polarization component has a Gaussian profile while the p -polarization component has an HG_{01} profile. (a) Spatial intensity profile of the s and p components. (b) H3 spot size for increasing intensity of the p generation field relative to the s generation field, calculated via the image moment (solid) and FWHM (dashed). (c)–(e) Calculated H3 emission spots. (f)–(h) Corresponding measured H3 emission spots from ZnO. White scale bars indicate 30 μm . (c) and (f) show emission when only the s field is present. (d) and (g) show emission when the s and p fields are $\pi/2$ out of phase. (e) and (h) show emission when the s and p fields are in phase.

clearly show HHG emission being minimal at the positions of maximal ellipticity.

To illustrate the capabilities of SPG for imaging we demonstrate spot size reduction below that of conventional HHG emission from ZnO using an 1800-nm driver. For this, we will focus on the H3 emission from the combination of an s -polarized fundamental Gaussian profile with a p -polarized HG_{01} profile, as shown in Fig. 3(a). The HG_{01} profile is obtained by using a phase step plate with the π phase jump centered on the optical axis. The alignment of two beams was optimized to ensure overlap and parallel propagation after recombination. Similar to the delay scans discussed before, the phase of the two beams was scanned using a delay stage; however, instead of recording the emission spectrum, the HHG emission profile was recorded using a camera. Additionally, the polarizer before the detector was rotated to be parallel with the s polarization.

We used the analytical model to evaluate the expected H3 emission spot size, which is shown in Fig. 3(b). We use two different metrics to evaluate the spot size, the full width at half maximum (FWHM) and the image moment (for details, see Supplemental Material [21]). The relative intensity is the intensity of the p component of the driver compared to the s component. We look at the two extremes of the two fields being in phase (blue) and $\lambda/4$ out of phase (red). The in-phase

spot size will simply increase with the relative intensity as the effective field strength at the edges of the spot is increased. For the out-of-phase case, we see that a reduction of the spot size can be achieved, which is caused by the edges of the spot becoming elliptically polarized. Comparing the image moment (solid line) and FWHM (dashed line), we see that for the image moment, the spot size reduction only happens for a range of relative intensities, while for the FWHM, the spot size decreases for much longer until it shoots up drastically. For the higher relative intensities, the ellipticity at the edge will be reduced, resulting in the formation of side peaks. These side peaks will result in the HHG emission being emitted throughout a bigger spatial region, however, the central peak still becomes narrower. When the intensity of the side peaks first exceeds half the intensity of the main peak the FWHM spot size is instantly greatly increased.

The calculated H3 emission spots for a relative intensity of 1 are shown in Figs. 3(c)–3(e), and the corresponding measured spots are shown in Figs. 3(f)–3(h). In Figs. 3(c) and 3(e), the emission from only the Gaussian *s*-polarized driver is shown, which corresponds to conventional Gaussian emission profiles. The spot size of the calculation was chosen to be in good agreement with the measurement. Good agreement is found between the calculations and experimental results for both the out-of-phase and in-phase spots. The out-of-phase spots are considerably narrower in the *y* direction, showing the increased spatial confinement of HHG emission. The out-of-phase spots instead show the greatly increased spot sizes. The maximum experimental spot size reduction found, evaluated via the image moment, was 30%, close to the predicted minimum. This demonstrates that our analytical model can predict the spatial HHG emission and that SPG enables localization of emission beyond that of conventional solid HHG emission.

The observed spot size reduction demonstrated here is a noticeable improvement, however, bigger improvements are desirable. Inherent to SPG is the need to balance the amplitude and phase of the electric field to achieve maximum ellipticity. To achieve sharp jumps in ellipticity, either sharp phase or amplitude jumps should be present, both of which are diffraction limited. This means that the local confinement of HHG emission with SPG is still diffraction limited. It is possible to make use of higher-order harmonics to improve the resolution further (see Supplemental Material [21]). However, this does not solve this inherent limitation.

To fully utilize SPG, we will have to move beyond point scanning and instead have to consider wide-field techniques, such as structured illumination microscopy (SIM) [12,39–41]. The key here is the observation that although the spatial confinement of HHG emission by SPG is limited, SPG does enable the creation of very sharp, predictable emission features. Conventional SIM uses frequency components in spatially structured illumination patterns to encode information about higher spatial frequencies of the sample into lower spatial frequency components (for details, see Supplemental Material [21]). Conventional SIM can increase the imaging resolution to twice the diffraction limit but is essentially still a diffraction-limited imaging method. However, it is possible to enhance the resolution of SIM beyond this by using nonlinear processes that introduce higher spatial frequency components into the illumination patterns. One way of achieving this is

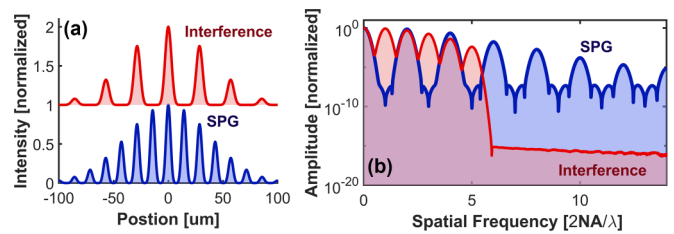


FIG. 4. Calculations of structured illumination of H5 with an interference grating and with an ellipticity grating for the same numerical aperture and beam angles. (a) Real-space intensity of H5. (b) Spatial frequencies of the emission, where λ is the driving wavelength.

by using the saturating intensity scaling of fluorescence or harmonic generation which is then referred to as saturated structured illumination microscopy (SSIM) [39,42]. By using SPG to create the illumination patterns in SIM (SPG-SIM), we can instead use the nonlinear ellipticity scaling to introduce higher spatial frequencies. SPG-SIM enables superresolution imaging without needing the high intensities required to reach the saturating regime, and alternatively, SPG-SIM can be used in conjunction with SSIM.

To illustrate the superresolution capabilities of SPG-SIM, Fig. 4 shows the calculated H5 emission of 2000 nm from respectively a conventional interference grating pattern and an SPG ellipticity-grating pattern. Both gratings are created by the overlap of two 2000 nm pulses, which have an angle between them [numerical aperture (NA) = 0.125]. The difference between the two gratings is that for the conventional grating, the beams have the same polarization while for the ellipticity grating they have orthogonal linear polarization. In SPG, the change from linear to circular happens within a half cycle of the field, instead of a full cycle, and this difference is reflected in Fig. 4 where the SPG emission profile has twice the number of peaks. The Fourier-transformed emission patterns are shown in Fig. 4(b). The interference grating shows a sharp cutoff at the diffraction limit of H5 as expected. The SPG pattern instead has spectral components exceeding this sharp cutoff, indicating its capabilities to be used for superresolution imaging. Realistic resolution improvements are difficult to deduce from these calculations as these will now depend on the noise in the imaging system. If we consider that any amplitude contributions above 10^{-5} can be detected, then SPG-SIM doubles the effective spatial frequencies in the illumination pattern which increases the maximum spatial frequency that can be detected from twice the diffraction for conventional SIM to three times the diffraction limit (for details, see Supplemental Material [21]). For this low NA example, the diffraction limit of H5 is 1600 nm, making the resolution limit of conventional SIM 800 nm, while the resolution of SPG-SIM goes up to about 530 nm. This relative increase stays consistent for a different NA, i.e., at an NA of 1, a resolution of 67 nm is possible. These calculations support the possibility of using SPG to enable wide-field superresolution imaging techniques for solids.

In conclusion, we introduced SPG for confining HHG below the diffraction limit, which can find application for high-resolution HHG imaging. Important for SPG is the common ellipticity response in solids where a strong suppression

of HHG emission is observed, qualitatively matching the atomic response. This ellipticity response was here qualitatively reproduced with SBE simulations without requiring detailed modeling of our material, indicating a dominance of the field characteristics. Spatial confinement of HHG by SPG can be predicted using a simple analytical framework. We demonstrated an H3 spot size reduction of about 30%, closely matching our calculated optimum. Exciting opportunities lie in applying SPG to higher-order harmonics and combining it with structured illumination. With these next steps, SPG can pave the way for high temporal and spatial resolution imaging in solids.

This work has been carried out at the Advanced Research Center for Nanolithography (ARCNL), a public-private partnership of the University of Amsterdam (UvA), the Vrije Universiteit Amsterdam (VU), the Netherlands Organisation for Scientific Research (NWO), and the semiconductor equipment manufacturer ASML, and was partly financed by

“Toeslag voor Topconsortia voor Kennis en Innovatie (TKI)” from the Dutch Ministry of Economic Affairs and Climate Policy. This manuscript is part of a project that has received funding from the European Research Council (ERC) under the European Union’s Horizon Europe research and innovation programme (Grant Agreement No. 101041819, ERC Starting Grant ANACONDA) and funded P.J.v.E. and partly P.M.K. The manuscript is also part of the VIDI research programme HIMALAYA with Project No. VI.Vidi223.133 financed by NWO, which funded B.d.K. and T.v.H. and partly funded P.M.K. Also, P.M.K. acknowledges support from the Open Technology Programme (OTP) by NWO, Grant No. 18703. E.B.M. and R.E.F.S. acknowledge support from Fellowship No. LCF/BQ/PR21/11840008 from “La Caixa” Foundation (ID 100010434). This research was supported by Grant No. PID2021-122769NB-I00 funded by MCIN/AEI/10.13039/501100011033. A.J.G. acknowledges support from Comunidad de Madrid through TALENTO Grant No. 2022-T1/IND-24102.

-
- [1] C. Heide, Y. Kobayashi, A. C. Johnson, F. Liu, T. F. Heinz, D. A. Reis, and S. Ghimire, Probing electron-hole coherence in strongly driven 2D materials using high-harmonic generation, *Optica* **9**, 512 (2022).
- [2] M. Hohenleutner, F. Langer, O. Schubert, M. Knorr, U. Huttner, S. W. Koch, M. Kira, and R. Huber, Real-time observation of interfering crystal electrons in high-harmonic generation, *Nature (London)* **523**, 572 (2015).
- [3] J. Zhang, Z. Wang, F. Lengers, D. Wigger, D. E. Reiter, T. Kuhn, H. J. Wärner, and T. T. Luu, High-harmonic spectroscopy probes lattice dynamics, *Nat. Photonics* **18**, 792 (2024).
- [4] M. R. Bionta, E. Haddad, A. Leblanc, V. Gruson, P. Lassonde, H. Ibrahim, J. Chaillou, N. Émond, M. R. Otto, Álvaro Jiménez-Galán, R. E. Silva, M. Ivanov, B. J. Siwick, M. Chaker, and F. Légaré, Tracking ultrafast solid-state dynamics using high harmonic spectroscopy, *Phys. Rev. Res.* **3**, 023250 (2021).
- [5] Z. Nie, L. Guery, E. B. Molinero, P. Jürgens, T. J. van den Hooven, Y. Wang, A. Jimenez Galan, P. C. M. Planken, R. E. F. Silva, and P. M. Kraus, Following the nonthermal phase transition in niobium dioxide by time-resolved harmonic spectroscopy, *Phys. Rev. Lett.* **131**, 243201 (2023).
- [6] P. J. van Essen, Z. Nie, B. de Keijzer, and P. M. Kraus, Toward complete all-optical intensity modulation of high-harmonic generation from solids, *ACS Photonics* **11**, 1832 (2024).
- [7] M. L. van der Geest, J. J. de Boer, K. Murzyn, P. Jürgens, B. Ehrler, and P. M. Kraus, Transient high-harmonic spectroscopy in an inorganic–organic lead halide perovskite, *J. Phys. Chem. Lett.* **14**, 10810 (2023).
- [8] B. de Keijzer, P. J. van Essen, and P. M. Kraus, Effect of photoexcitation on high-harmonic generation in semiconductors, *J. Opt. Soc. Am. B* **41**, 1754 (2024).
- [9] M. Garg, M. Zhan, T. T. Luu, H. Lakhota, T. Klostermann, A. Guggenmos, and E. Goulielmakis, Multi-petahertz electronic metrology, *Nature (London)* **538**, 359 (2016).
- [10] M. Sivilis, M. Taucer, G. Vampa, K. Johnston, A. Staudte, A. Y. Naumov, D. Villeneuve, C. Ropers, and P. Corkum, Tailored semiconductors for high-harmonic optoelectronics, *Science* **357**, 303 (2017).
- [11] S. D. C. Roscam Abbing, R. Kolkowski, Z.-Y. Zhang, F. Campi, L. Lötgering, A. F. Koenderink, and P. M. Kraus, Extreme-ultraviolet shaping and imaging by high-harmonic generation from nanostructured silica, *Phys. Rev. Lett.* **128**, 223902 (2022).
- [12] N. Sun, Y. Jia, S. Bai, Q. Li, L. Dai, and J. Li, The power of super-resolution microscopy in modern biomedical science, *Adv. Colloid Interface Sci.* **314**, 102880 (2023).
- [13] S. W. Hell and J. Wichmann, Breaking the diffraction resolution limit by stimulated emission: stimulated-emission-depletion fluorescence microscopy, *Opt. Lett.* **19**, 780 (1994).
- [14] H. Blom and J. Widengren, Stimulated emission depletion microscopy, *Chem. Rev.* **117**, 7377 (2017).
- [15] S. T. Hess, T. P. Girirajan, and M. D. Mason, Ultra-high resolution imaging by fluorescence photoactivation localization microscopy, *Biophys. J.* **91**, 4258 (2006).
- [16] J. Xu, H. Ma, and Y. Liu, Stochastic optical reconstruction microscopy (STORM), *Curr. Protoc. Cytometry* **2017**, 12.46.1 (2017).
- [17] K. Murzyn, M. L. S. van der Geest, L. Guery, Z. Nie, P. van Essen, S. Witte, and P. M. Kraus, Breaking Abbe’s diffraction limit with harmonic deactivation microscopy, *Sci. Adv.* **10**, eadp3056 (2024).
- [18] P. B. Corkum, N. H. Burnett, and M. Y. Ivanov, Subfemtosecond pulses, *Opt. Lett.* **19**, 1870 (1994).
- [19] G. Sansone, E. Benedetti, F. Calegari, C. Vozzi, L. Avaldi, R. Flammini, L. Poletto, P. Villoresi, C. Altucci, R. Velotta, S. Stagira, S. D. Silvestri, and M. Nisoli, Isolated single-cycle attosecond pulses, *Science* **314**, 443 (2006).
- [20] O. Masihzadeh, P. Schlup, and R. A. Bartels, Enhanced spatial resolution in third-harmonic microscopy through polarization switching, *Opt. Lett.* **34**, 1240 (2009).
- [21] See Supplemental Material at <http://link.aps.org/supplemental/10.1103/PhysRevResearch.7.L012063> for details on the experiment, simulation, and analyses, which includes Refs. [22–31].

- [22] P. Antoine, A. L'Huillier, M. Lewenstein, P. Salières, and B. Carré, Theory of high-order harmonic generation by an elliptically polarized laser field, *Phys. Rev. A* **53**, 1725 (1996).
- [23] X. Zhang, J. Li, Z. Zhou, S. Yue, H. Du, L. Fu, and H. G. Luo, Ellipticity dependence transition induced by dynamical Bloch oscillations, *Phys. Rev. B* **99**, 014304 (2019).
- [24] T. Tamaya, A. Ishikawa, T. Ogawa, and K. Tanaka, Higher-order harmonic generation caused by elliptically polarized electric fields in solid-state materials, *Phys. Rev. B* **94**, 241107(R) (2016).
- [25] R. Hollinger, P. Herrmann, V. Korolev, M. Zapf, V. Shumakova, R. Rder, I. Uschmann, A. Puglys, A. Baltuka, M. Zrch, C. Ronning, C. Spielmann, and D. Kartashov, Polarization dependent excitation and high harmonic generation from intense mid-IR laser pulses in ZnO, *Nanomaterials* **11**, 4 (2021).
- [26] N. Tancogne-Dejean, O. D. Mcke, F. X. Krtner, and A. Rubio, Ellipticity dependence of high-harmonic generation in solids originating from coupled intraband and interband dynamics, *Nat. Commun.* **8**, 745 (2017).
- [27] C. Heide, Y. Kobayashi, D. R. Baykusheva, D. Jain, J. A. Sobota, M. Hashimoto, P. S. Kirchmann, S. Oh, T. F. Heinz, D. A. Reis, and S. Ghimire, Probing topological phase transitions using high-harmonic generation, *Nat. Photon.* **16**, 620 (2022).
- [28] N. Klemke, O. D. Mcke, A. Rubio, F. X. Krtner, and N. Tancogne-Dejean, Role of intraband dynamics in the generation of circularly polarized high harmonics from solids, *Phys. Rev. B* **102**, 104308 (2020).
- [29] F. Sekiguchi, M. Sakamoto, K. Nakagawa, H. Tahara, S. A. Sato, H. Hirori, and Y. Kanemitsu, Enhancing high harmonic generation in GaAs by elliptically polarized light excitation, *Phys. Rev. B* **108**, 205201 (2023).
- [30] Y. S. You, D. A. Reis, and S. Ghimire, Anisotropic highharmonic generation in bulk crystals, *Nature Phys.* **13**, 345 (2017).
- [31] N. Yoshikawa, T. Tamaya, and K. Tanaka, Optics: High-harmonic generation in graphene enhanced by elliptically polarized light excitation, *Science* **356**, 736 (2017).
- [32] C. Liu, Y. Zheng, Z. Zeng, and R. Li, Effect of elliptical polarization of driving field on high-order-harmonic generation in semiconductor ZnO, *Phys. Rev. A* **93**, 043806 (2016).
- [33] M. Möller, Y. Cheng, S. D. Khan, B. Zhao, K. Zhao, M. Chini, G. G. Paulus, and Z. Chang, Dependence of high-order-harmonic-generation yield on driving-laser ellipticity, *Phys. Rev. A* **86**, 011401(R) (2012).
- [34] E. Goulielmakis and T. Brabec, High harmonic generation in condensed matter, *Nat. Photonics* **16**, 411 (2022).
- [35] R. E. F. Silva, F. Martín, and M. Ivanov, High harmonic generation in crystals using maximally localized Wannier functions, *Phys. Rev. B* **100**, 195201 (2019).
- [36] E. B. Molinero, Álvaro Jiménez-Galán, and R. E. F. Silva, Wannier approach to the semiconductor Bloch equations, in *High-Order Harmonic Generation in Solids* (World Scientific, Singapore, 2024), Chap. 3, pp. 50–71.
- [37] P. A. Rodnyi and I. V. Khodyuk, Optical and luminescence properties of zinc oxide, *Opt. Spectrosc.* **111**, 776 (2011).
- [38] I. Kimel and L. R. Elias, Relations between Hermite and Laguerre Gaussian modes, *IEEE J. Quantum Electron.* **29**, 2562 (1993).
- [39] M. G. Gustafsson, Nonlinear structured-illumination microscopy: Wide-field fluorescence imaging with theoretically unlimited resolution, *Proc. Natl. Acad. Sci. USA* **102**, 13081 (2005).
- [40] R. Heintzmann and T. Huser, Super-resolution structured illumination microscopy, *Chem. Rev.* **117**, 13890 (2017).
- [41] Y. Wu and H. Shroff, Faster, sharper, and deeper: structured illumination microscopy for biological imaging, *Nat. Methods* **15**, 1011 (2018).
- [42] J. J. Field, K. A. Wernsing, S. R. Domingue, A. M. Motz, K. F. DeLuca, D. H. Levi, J. G. DeLuc, M. D. Young, J. A. Squier, and R. A. Bartels, Superresolved multiphoton microscopy with spatial frequency-modulated imaging, *Proc. Natl. Acad. Sci. USA* **113**, 6605 (2016).